Spin wave dispersion of ultra-low damping hematite (α-Fe_2O_3) at GHz frequencies

Mohammad Hamdi [1,*] Ferdinand Posva [1] and Dirk Grundler [1,2,†]

[1] *École Polytechnique Fédérale de Lausanne (EPFL), Institute of Materials, Laboratory of Nanoscale Magnetic Materials and Magnonics, CH-1015 Lausanne, Switzerland*

[2] *École Polytechnique Fédérale de Lausanne (EPFL), Institute of Electrical and Micro Engineering, CH-1015 Lausanne, Switzerland*

(Received 22 December 2022; accepted 1 May 2023; published 30 May 2023)

Low magnetic damping and high group velocity of spin waves (SWs) or magnons are two crucial parameters for functional magnonic devices. Magnonics research on signal processing and wave-based computation at GHz frequencies focused on the artificial ferrimagnetic garnet $Y_3Fe_5O_{12}$ (YIG) so far. We report on spin wave spectroscopy studies performed on the natural mineral hematite (α-Fe_2O_3), which is a canted antiferromagnet. By means of broadband GHz spectroscopy and inelastic light scattering, we determine a damping coefficient of 1.1×10^{-5} and magnon group velocities of a few 10 km/s, respectively, at room temperature. Covering a large regime of wave vectors up to $k \approx 24\,\mathrm{rad}/\mu\mathrm{m}$, we find the exchange stiffness length to be relatively short and only about 1 Å. In a small magnetic field of 30 mT, the decay length of SWs is estimated to be 1.1 cm similar to the best YIG. Still, inelastic light scattering provides surprisingly broad and partly asymmetric resonance peaks. Their characteristic shape is induced by the large group velocities, low damping, and distribution of incident angles inside the laser beam. Our results promote hematite as an alternative and sustainable basis for magnonic devices with fast speeds and low losses based on a stable natural mineral.

DOI: 10.1103/PhysRevMaterials.7.054407

I. INTRODUCTION

Spin waves (magnons) are collective spin excitations in magnetically ordered materials. They exhibit promising functionalities for information transmission and processing at GHz frequencies [1–3]. To realize energy efficient magnonic circuits [1,2,4–6] isotropic spin wave (SW) dispersion relations, high group velocities, and low magnetic damping are essential. Until today, the artificial garnet $Y_3Fe_5O_{12}$ (YIG) [7] played a key role for the exploration of magnonics functionalities [8]. Already in 1961, M. Sparks *et al.* coined the phrase that YIG was to ferromagnetic resonance research what the fruit fly was to genetics research [9]. This was particularly true for high-quality YIG grown by liquid phase epitaxy on the wafer scale [8,10]. However, in a ferrimagnetic material like YIG, magnon bands in the regime of small wave vectors, k, and low GHz frequencies are inherently anisotropic due to the dipolar interaction between spins. To overcome this, a lot of effort has been put into the development of microwave-to-magnon transducers, which allow for the excitation of exchange dominated SWs with isotropic properties at high frequencies [11–13]. Some of these transducers involved additional ferromagnets and showed either narrow excitation bands [11,12] or required an applied field of up to 0.1 T [13] to enable fast spin waves in thin YIG. The reported velocities amounted to a few km/s. There is a quest for materials, which offer fast spin waves over broad frequency and wave vector regimes accessible by transmission lines and coplanar waveguides (CPWs) without added ferromagnetic components.

In antiferromagnetic (AFM) materials, exchange interaction dominates the dispersion relation already at small wave vectors k. The dipolar interactions are virtually absent due to net zero magnetization. Still, SWs can propagate with high group velocities. Values similar to thick YIG [8,14] and as high as 30 km/s have been reported [15–18]. However, the challenge with most AFMs is their net zero magnetization and sub-THz frequencies, which make on-chip integration hard due to lack of efficient CPWs and THz sources (THz gap) [19,20]. Recently, the natural mineral and canted antiferromagnet hematite (α-Fe_2O_3) [21] gained particular attention for magnonics [22,23] after the observation of long-distance spin transport [24,25] and enhanced spin pumping [26]. It is known that, due to extremely low anisotropy in the basal plane [21,27,28], in the canted phase [Figs. 1(a) and 1(b)] one branch of the magnon modes resides at around 10 GHz at small k. Depending on the purity of hematite crystals, a damping coefficient as low as 7.8×10^{-6} was reported for the magnetic resonance [29]. The hematite's finite net magnetization and strikingly small damping of below 10^{-5} hence make it suitable for magnonic applications. They allow for inductive coupling to CPWs and long-distance SW transport, respectively. However, there is no experiment reporting a measured SW dispersion for k values accessible by CPWs with integrated microwave-to-magnon transducers [11–13]. The dispersion measured over a large wave vector regime is of fundamental importance as it allows one to quantify the exchange stiffness length l_e with large precision. l_e is the key parameter to estimate the maximum possible spin wave velocity of hematite in the GHz frequency regime.

*mohammad.hamdi@epfl.ch, mohamad.hamdi90@gmail.com
†dirk.grundler@epfl.ch

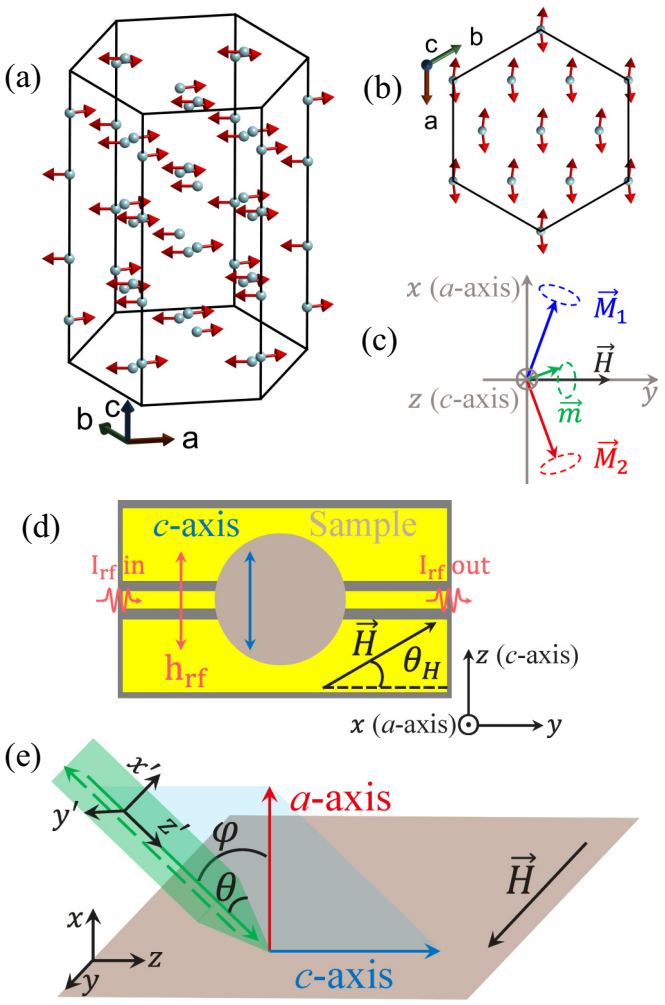

FIG. 1. Hexagonal unit cell of the crystal structure of hematite from (a) the side and (b) top view. The cyan spheres and red arrows indicate the Fe atoms and the spins associated with them, respectively (oxygen atoms are not shown). We depict the canted antiferromagnetic state above the Morin temperature for which the sublattice spins lie in the c plane along the a axis with a small canting. They give rise to sublattice magnetization vectors $\mathbf{M}_1$ and $\mathbf{M}_2$. (c) Sketch of the low-frequency quasiferromagnetic mode where a small magnetization (green arrow), $\mathbf{m}$, precesses elliptically around the applied field (black arrow), $\mathbf{H}$. (d) Schematics of the flip-chip VNA measurement. The sample (gray disk) is placed on a CPW. The static magnetic field, $\mathbf{H}$, is applied in the a plane and with an angle, θ_H, to the normal of the c axis of the crystal. The rf magnetic field (orange double-headed arrow), $\mathbf{h}_{\rm rf}$, of the CPW is parallel to the c axis. (e) Sketch of the BLS configuration. The magnetic field, $\mathbf{H}$, is applied perpendicular to c axis in the a plane. The laser light (green) forms a Gaussian beam and is focused on the surface of the sample (gray). The cone angle of the objective lens is θ. The incident laser light with an incidence angle, φ is scattered by magnons. We measure in back-scattering geometry (dashed green arrow).

Here, we study the magnon band structure of bulk hematite at different wave vectors k by means of broadband microwave spectroscopy and k-resolved inelastic Brillouin light scattering (BLS) (Fig. 1). Using a CPW in flip-chip configuration we extract a magnetic damping parameter of 1.12×10^{-5}, which is similar to the best YIG reported in Ref. [30]. Still, the measured spectra with BLS show broad line widths. Our modeling substantiates that the linewidth is explained by the SW dispersion relation, the large SW velocity and the Gaussian profile of the laser used for inelastic light scattering. The data substantiate a high group velocity of 10 km/s for $k = 2.5$ rad/μm, which are excited easily by a μm-sized CPW [23,31]. In an applied field of 90 mT, the velocity increases to 16 km/s near $k = 5$ rad/μm and levels off to 23.3 km/s for $k \geqslant 25$ rad/μm. The latter value has routinely been realized by transducers. Our findings substantiate hematite as a very promising candidate for a sustainable future of magnonics as its growth avoids the lead-based synthesis route used for high-quality YIG [7,30].

II. PROPERTIES OF HEMATITE

We first briefly review the relevant magnetic properties of α-Fe_2O_3. Hematite is the stable end product of oxidation of magnetite [32] and known for its great abundance as well as stability in an aqueous environment [33]. It is an insulating antiferromagnet (AFM) with a corundum crystal structure. The arrangement of the magnetic atoms of Fe in the crystal is shown in Fig. 1(a) [34]. At room temperature and above the Morin transition temperature of $T_{\rm M} = 262$ K the Fe^{+3} magnetic moments lie in the c plane due to an easy plane anisotropy, $H_{\rm A}$, and stack antiferromagnetically along the c axis [Fig. 1(a)] [21,28]. Within the c plane, there is a weak sixfold anisotropy around the c axis, $H_{\rm a}$, which favors the magnetic moments to align with the a axes [Fig. 1(b)]. The magnetic moments of the two AFM sublattices are slightly canted away from the a axis by the Dzyaloshinskii-Moriya (DM) interaction [Fig. 1(b)], resulting in a weak magnetic moment, $\mathbf{m}$, perpendicular to both a and c axes at equilibrium [21,28]. The magnetization amounts to about 2 kA/m [32]. In Refs. [35–39] the authors discussed domain nucleation and domain wall propagation in bulk hematite crystals. They reported that in an opposing field of about 2.5 mT the domain structure of a large sample was removed except for some localized regions that were probably the sites of crystal defects. Below we evaluate spectra taken in fields of 50 mT and larger. Thereby we intend to minimize (avoid) effects of domains. The magnetization dynamics of hematite in this weak ferromagnetic state offers two modes namely the quasiferromagnetic mode (qFM or low-frequency mode) and quasiantiferromagnetic mode (qAFM or high-frequency mode) [21,27,28].

All measurements are performed on an a plane natural crystal of hematite, which is available commercially [40]. The qAFM mode of our sample is reported in Ref. [41]. Here, we explore the qFM mode schematically depicted in Fig. 1(c). The canted AFM sublattice magnetization vectors precess elliptically around their equilibrium direction. This results in an elliptical precession of the weak magnetic moment, $\mathbf{m}$ [green arrow in Fig. 1(c)], around the applied field, $\mathbf{H}$ [21,27,28]. The frequency of the qFM mode was derived by Pincus [21,27] according to

$$f_r = \frac{|\gamma|\mu_0}{2\pi}\sqrt{H\sin\xi(H\sin\xi + H_{\rm D}) + 2H_{\rm E}(H_{\rm a} + H_{\rm ME})}, \quad (1)$$

where, γ, μ_0, H_E, H_D, and H_{ME} is the electron gyromagnetic ratio, vacuum permeability, exchange, DM and spontaneous magnetoelastic effective field, respectively. $\xi = \pi/2 - \theta_H$ is the polar angle between **H** and the c axis (z direction). We define θ_H in Fig. 1(d). Fink [42] derived the dynamic susceptibility $\chi_{zz}(f, f_r)$ for the qFM mode. The real and imaginary parts read

$$\mathrm{Re}[\chi_{zz}(f, f_r)] = \frac{\left(f_r^2 - f^2\right) f_r^2}{\left(f_r^2 - f^2\right)^2 + \Delta f^2 f^2} \quad \text{and} \tag{2}$$

$$\mathrm{Im}[\chi_{zz}(f, f_r)] = \frac{f f_r^2 \Delta f}{\left(f_r^2 - f^2\right)^2 + \Delta f^2 f^2}, \tag{3}$$

respectively. Here, f is the frequency of the radio frequency (rf) magnetic field $\mathbf{h}_{rf}$ [Fig. 1(d)]. The frequency linewidth, Δf, is related to the magnetic damping parameter, α, by

$$\Delta f \approx 2\alpha H_E(\gamma/2\pi), \tag{4}$$

for $H \ll H_E$. Unlike ferromagnets and uniaxial antiferromagnets, the resonance line width of a canted antiferromagnet does not depend on f_r and is governed by the field-independent exchange frequency. Following Turov [15,16], the SW dispersion of the qFM mode for hematite near $k = 0$ is given by

$$f_m(k) = \frac{|\gamma|\mu_0}{2\pi}\sqrt{H(H + H_D) + 2H_E(H_a + H_{ME} + Ak^2)}, \tag{5}$$

where $A = H_E l_e^2$ is the dispersion coefficient and l_e is the effective magnetic lattice parameter or exchange stiffness length. For Eq. (5), we considered the experimental geometry for k-resolved BLS measurements with an angle $\xi = \pi/2$ as described below.

III. EXPERIMENTAL TECHNIQUES

The broadband microwave spectroscopy was conducted at room temperature above T_M [Fig. 1(d)]. The disk-shaped a plane α-Fe_2O_3 crystal had a diameter of 2.3 mm and thickness of 0.5 mm. Measurements were done in flip-chip configuration for which the sample was placed on a CPW with signal (ground) line width of 165 μm (295 μm). The a axis of the crystal was perpendicular to the disk plane. The c axis was in the plane and perpendicular to the CPW axis. Injecting a radio-frequency (rf) current, I_{rf}^{in}, into the CPW by port 1 of a vector network analyzer (VNA) induced the dynamic magnetic field $\mathbf{h}_{rf}$ (orange double-head arrow). The rf current was collected on the other end of the CPW by port 2 of the VNA (I_{rf}^{out}). The static magnetic field, **H**, was applied in the a plane of the crystal in all VNA measurements [yz plane in Fig. 1(d)]. For the angle-dependent measurements an external field of 90 mT was applied and the angle, θ_H, was varied in steps of $\Delta\theta_H = 2^\circ$. In case of field sweep measurements, the applied field angle was perpendicular to the c axis and in the a plane of the crystal ($\theta_H = 0$ deg). The field amplitude was varied in steps of $\mu_0\Delta H = 0.5$ mT.

Wave-vector-resolved BLS measurements were done for $\theta_H = 0$ deg on a piece of the same crystal in back-scattering geometry [Fig. 1(e)] using a green laser with wavelength, $\lambda = 532$ nm and wave vector $k_0 = 2\pi/\lambda = 11.81$ rad/μm. The external field was applied in the a plane and perpendicular to c axis. The sample for BLS was irregularly shaped. We ensured that it was tilted with respect to the incident laser beam along the y axis in such a way that the laser beam remained in the xz plane formed by the a and c axis. Since the penetration depth of the green laser in hematite is on the order of 75 nm [43], linear momentum conservation holds only for the in-plane component of the transferred wave vectors. Therefore, we define the transferred momentum from the light to magnons along the c axis as $k_z = 2(k_0 \sin\varphi + k_x' \cos\varphi)$, where φ is the angle between the incident beam and the normal to the plane of the sample (a plane) [44]. We assume a Gaussian beam profile giving rise to a Fourier transform of the beam intensity I as

$$I(k_x') = e^{k_x'^2 w_0^2/2} \tag{6}$$

with $w_0 = \frac{2}{k_0 NA}$. NA is the numerical aperture of the lens [45,46]. The momentum k_x' has a projection on the z direction due to the focusing of the beam.

IV. BROADBAND MICROWAVE SPECTROSCOPY DATA

Field-dependent VNA spectra are shown in Fig. 2(a). We depict the imaginary part of the measured quantity $U_{exp}(f, H) = i\ln[S_{21}(f, H)/S_{21}(f, H = 0)]$ in a color-coded plot, where S_{21} is the complex scattering parameter measured by the VNA at a given field, H. We identify two branches, which we label f_1 and f_2 for positive fields. For a detailed analysis, we consider that the parameter U contains the susceptibility χ of the sample [47,48] and the electromagnetic response of the rf circuit used in the flip-chip method. To account for the different contributions, we follow Refs. [47,48] and fit the measured U_{exp} with

$$U_{Fit} = C[1 + \chi_0 + \chi(f, f_1, \Delta f_1)e^{i\phi_1} + \chi(f, f_2, \Delta f_2)e^{i\phi_2}] \tag{7}$$

as shown in Figs. 2(b) and 2(c) (black lines). C is a real-numbered scaling parameter, χ_0 is a complex-numbered offset parameter, and ϕ_i are phase shift adjustments ($i = 1, 2$). Using Eq. (7), we extract the resonance frequencies and linewidths Δf_i for the two modes labeled by f_1 and f_2. In Figs. 2(b) and 2(c), we display the measured imaginary and real parts of U_{exp} with red symbols. In Figs. 2(d) and 2(e), we show the extracted real and imaginary parts together with the total susceptibilities (gray lines) from which the two resonant modes are identified. Their frequencies extracted for different H are depicted in Fig. 2(a) with solid red circles and magenta triangles. We focus on spectra obtained in fields larger than 50 mT.

The blue line in Fig. 2(a) results from fitting Eq. (1) to branch f_1 with $\xi = \pi/2$. From the fit, we obtain $\mu_0 H_E = 1003.61$ T, $\mu_0 H_D = 2.34$ T, and $\mu_0(H_a + H_{ME}) = 88.64$ μT. Using Eq. (4) and the experimental value of $\Delta f_1 = 0.63$ GHz for branch f_1, we extract a damping parameter of $\alpha = 1.12\times10^{-5}$. This value is similar to the best value reported for YIG in Ref. [30]. The branch f_2 will be discussed later.

Angle-dependent VNA spectra are shown in Fig. 3. To enhance the signal-to-noise ratio, we depict $\Delta|S_{12}| =$

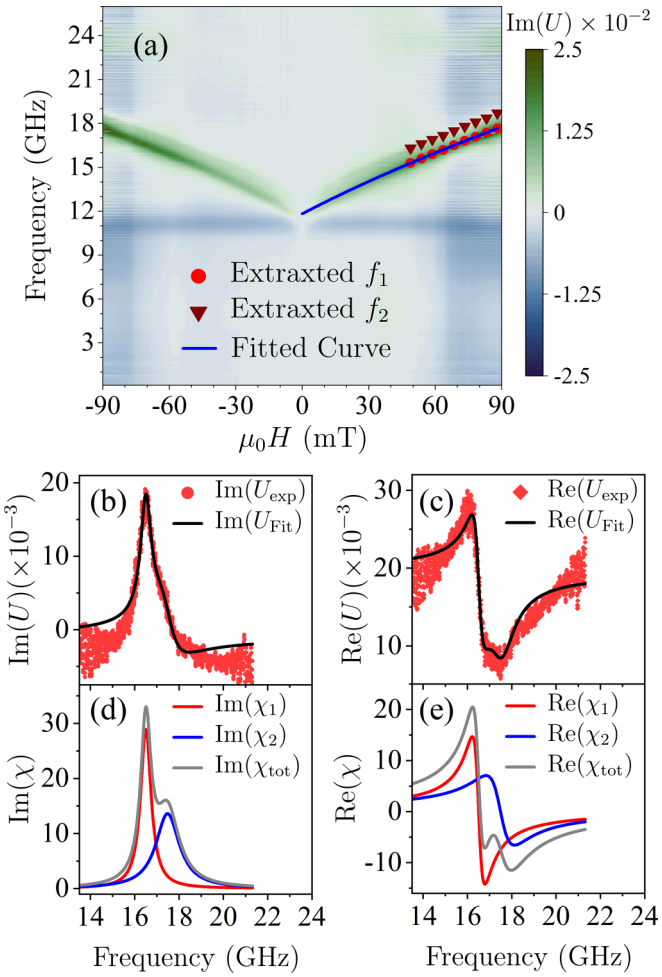

FIG. 2. (a) Color-coded field-dependent $\mathrm{Im}(U_{\mathrm{exp}})$ parameter measured on the sample as indicated in Fig. 1(d) with $\theta_H = 0$ deg. Solid red circles and wine triangles are the frequencies extracted by fitting Eq. (7) to the data. The blue solid line is obtained by fitting Eq. (1) with extracted f_1 values. (b) Imaginary and (c) real part of U_{exp} (red symbols) and U_{fit} (black curves) for 70 mT. (d) Imaginary and (e) real parts of χ_1 (red curve), χ_2 (blue curve), and their sum (gray curve) for 70 mT.

$|S_{12}(H + \Delta H) - S_{12}(H)|$. For such data, a zero-crossing (highlighted by the red curve) represents the resonance frequency. The spectra show a twofold symmetry as expected for the c axis being in the plane of the applied magnetic fields. Introducing the extracted parameters discussed above, Eq. (1) models well the resonance frequency of branch f_1 as a function of angle θ_H (red line). The angular dependency is hence consistent with the effective anisotropy field extracted from the field-dependent data.

V. BLS DATA

The BLS spectra for different values of incident angle, φ, are shown in Fig. 4(a). Black symbols in Fig. 4(b) depict the frequency position of the maximum BLS peak as a function of wave vector calculated from the incidence angles shown in the legend of Fig. 4(a). The red curve in Fig. 4(b) is obtained by considering first the material parameters ob-

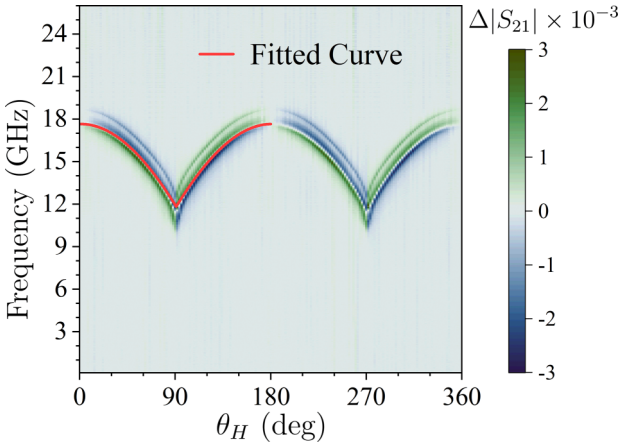

FIG. 3. Color-coded neighbor subtracted angle-dependent VNA-FMR spectra measured on the sample as indicated in Fig. 1(d) with $\mu_0 H = 90$ mT. The orange curve is calculated by Eq. (1) using extracted material parameters.

tained from VNA measurements and then fitting Eq. (5) to the black symbols in the same graph. We obtain a dispersion coefficient of $\mu_0 A = 9.153 \times 10^{-6}$ T.μm^2, which leads to an exchange stiffness length of $l_e = 0.955$ Å. Using Eq. (5) and the obtained parameters we calculate the SW group velocity, v_g, for $\mu_0 H = 90$ mT [blue line in Fig. 4(c)]. The velocity v_g increases significantly with k and levels off at 23.3 km/s. Such a high group velocity is the direct result of the strong exchange interaction and at the same time vanishingly small net magnetization. Microstructured CPWs used in magnonics offer SW wave vectors around $k = 2.5$ rad/μm [23,31]. For such a value k, the qFM spin wave in hematite exhibits a group velocity of $v_g = 10$ km/s similar to SWs in thick YIG and about a factor of 10 larger compared to ultrathin YIG [49]. The decay length of the SWs is given by $l_d = v_g \tau$, where $\tau = (1/2\pi\alpha f_m(k))$ is the relaxation time of the SW. For 30 mT applied field and $k = 2.5$ rad/μm we calculate $v_g = 13.4$ km/s and $\tau = 840.6$ ns, which leads to $l_d = 11.3$ mm, again similar to thick YIG. This is due to low damping and high group velocity of the qFM spin waves in hematite.

Despite the small damping of the hematite sample measured by the VNA, the resonance peaks of the qFM mode in the BLS spectra show a large width of 10–20 GHz, which is much broader than VNA measurements (0.63 GHz). Furthermore, the BLS peak taken at nearly normal incidence of the laser beam (e.g., at $\varphi = 0$ deg or 5 deg) shows a strong asymmetric shape. As φ increases, the intensity of the prominent peak reduces and it becomes more and more symmetric. The resolution of the BLS equipment is much better than 0.63 GHz. However, the BLS detection does not conclude a high damping. To understand these observations, we calculated the partial density of states (pDOS) by considering the magnon dispersion relation and the Gaussian beam profile according to

$$\mathrm{pDOS}(f, \varphi) = -\frac{1}{\pi} \int_{-\infty}^{+\infty} dk_x' \cos\varphi \, \mathrm{Im}\left[\frac{I(k_x')}{f - f_m(k) + i\Delta f}\right]. \tag{8}$$

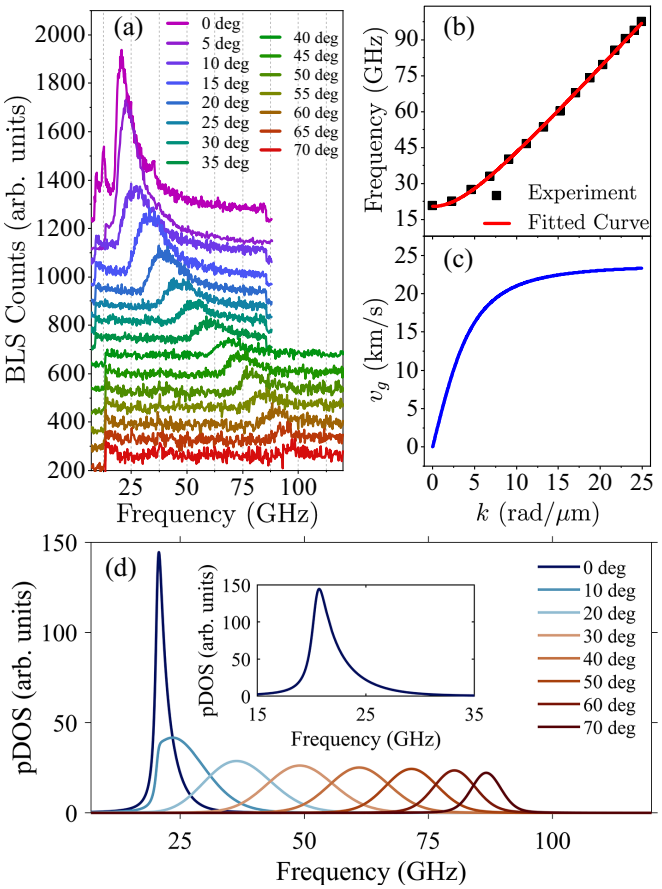

FIG. 4. (a) BLS spectra for different incident angles, φ, measured as indicated in Fig. 1(e) with $\mu_0 H = 90$ mT. (b) Extracted peak maxima frequencies (black squares) as a function of corresponding transferred wave vector, k and fitted dispersion relation (red curve) by Eq. (5). (c) Group velocity and (d) partial density of states obtained from the fitted magnon dispersion at $\mu_0 H = 90$ mT. Inset in (d) depicts pDOS for $\varphi = 0$ degree.

Assuming only fully back-reflected light we have $k = 2(k_0 \sin\varphi + k'_x \cos\varphi)$. $\Delta f = 0.63$ GHz, determined by VNA, is the resonance broadening due to the damping given by Eq. (4). The numerical aperture of the objective lens was $NA = 0.18$. The calculated pDOS for different incident angles is plotted in Fig. 4(d). Comparing Figs. 4(a) and 4(c), the experimental BLS peaks are broad because they contain a certain frequency regime of the band structure, which is determined by the Gaussian wave vector distribution of $k = 2k_0 \sin\varphi + \Delta k$. The central wave vector is $k_c = 2k_0 \sin\varphi$ and the distribution function for $\Delta k = 2k'_x \cos\varphi$ is given by $I(k'_x)$ [Eq. (6)]. We attribute the broad BLS peaks hence to the high group velocity of magnons, which leads to a peak width proportional to $v_g \times \Delta k$. The asymmetry of BLS peaks for small φ can be understood in terms of the van Hove singularity of the pDOS near $k = 0$. As φ increases, the part of the band structure, which is relevant for the collected light shifts away from $k = 0$. Consequently, the peak gets more symmetric with φ. The peak intensity reduces with φ due to the factor $\cos\varphi$ in Eq. (8). We note that Eq. (8) does not include all possible scattering processes. Still it provides a good qualitative understanding about the contributions giving rise to the characteristics shape and signal strength of BLS peaks as a function of φ.

VI. DISCUSSION

The branch of mode f_2 in Fig. 2(a) is higher by about $\delta f = 1$ GHz than f_1 at the same field H. A second branch was reported also in Ref. [41]. Here the authors studied the qAFM mode at zero field and assumed a distribution of magnetic domains. We applied a large enough magnetic field to avoid domains. A domain formation can not explain our second branch. Another possibility for f_2 is a standing wave along the thickness of the sample or a SW excited with a discrete wave vector coming from the CPW. However, for these cases a quantitative estimate based on the magnon dispersion obtained with BLS [Eq. (5)] led to a frequency separation of much smaller than 1 GHz.

The remaining explanation for f_2 is a nonuniform magnetoelastic field in the sample induced when fixing the sample on the CPW. We attribute the observed frequency splitting to different strains in different parts of the sample that is either in contact with the CPW conductors or floating on the CPW gaps. A difference of $\mu_0 \delta H_{\mathrm{ME}} = 24\,\mu$T would account for $\delta f = f_2 - f_1 = 1$ GHz. The effect of magnetoelastic interaction by unidirectional compression, $\mathbf{p}$, in the basal plane of the crystal, on the qFM mode is given by replacing $\mu_0 H_{\mathrm{ME}}$ with $\mu_0 H'_{\mathrm{ME}} = \mu_0 H_{\mathrm{ME}} - Rp\cos 2\psi$ [50,51]. Here, $R = 287\,\mu$T/bar [51] is a coefficient determined by the elastic and magnetoelastic parameters of the crystal and $\psi = \pi/2$ is the angle between $\mathbf{p}$ and $\mathbf{H}$. Using $\mu_0 \delta H_{\mathrm{ME}} = Rp$ we obtain $p = 0.084$ bar. This value corresponds to a force of 14.6 mN on the parts of the crystal that are in contact with the CPW conductors. The evaluated force is one order of magnitude smaller than the weight of our sample and indicates the known sensitivity of hematite towards magnetoelastic effects.

From our experiments, we do not determine H_{a} and H_{ME} separately as they enter Eq. (1) in the same way. To separate the small H_{a} from H_{ME} an angle-dependent VNA measurement with the magnetic field applied in the c plane of the crystal would be required. The existing sample was not suitable for that.

Our BLS data were acquired on an a-plane crystal over a large wave vector regime with k along the c axis. We evaluate a value of $l_{\mathrm{e}} = 0.96$ Å. The authors of Ref. [23] extracted an exchange stiffness length l_{e} of 1.2 Å when exploring c-plane hematite. The precise determination of l_{e} along different crystal directions is of key importance as it determines the corresponding SW group velocity.

Contrary to the ferrimagnetic YIG, dipolar effects are not expected to play an important role in SW dispersion of hematite. Hence, hematite thin films can provide similarly large spin wave velocities as reported here for the bulk crystal. As a consequence, they potentially outperform YIG thin films concerning speed and decay lengths at wave vectors which are realized by the state-of-the-art transducers. Furthermore, hematite is based on earth-abundant elements and as an end product of oxidation of magnetite a stable natural mineral suggesting sustainable synthesis routes.

VII. CONCLUSION

We have measured the magnon dispersion relation of hematite for wave vectors k, which are relevant for timely experiments in magnonics. The damping coefficient of the studied natural crystal was 1.1×10^{-5} at room temperature. This value is only 40% larger than the best value reported for pure hematite and is already as good as the best YIG. The estimated spin wave decay length for $k = 2.5\,\mathrm{rad}/\mu\mathrm{m}$ is larger than 1 cm in a small magnetic field. In optimized thin films, current microwave-to-magnon transducers are expected to achieve larger group velocities in hematite than in YIG. The reported properties suggest that hematite can become the fruit fly of sustainable modern magnonics.

Note added. Recently, completing the manuscript about our experiments on hematite [22], we became aware of Ref. [23]. The authors measured group velocities and the spin wave dispersion via CPWs integrated to c-plane hematite for $1\ \mathrm{rad}/\mu\mathrm{m} \leqslant k \leqslant 3.5\,\mathrm{rad}/\mu\mathrm{m}$. Our measurements address a different crystal direction in a-plane hematite while covering a seven times larger regime of k values by means of BLS. The reported parameters l_e are decisive to estimate velocities of SWs in hematite for magnons at GHz frequencies propagating in different directions. We note that in Ref. [17], the authors applied inelastic neutron scattering to a bulk hematite crystal and addressed much higher frequencies $\geqslant 2.4\,\mathrm{THz}$ (wave vectors $\geqslant 5.4\times10^{2}\,\mathrm{rad}/\mu\mathrm{m}$). Their reported velocities amounted to $v_{\parallel} = 22.4\,\mathrm{km/s}$ for k parallel to the c axis and $v_{\perp} = 30\,\mathrm{km/s}$ for k perpendicular to c axis.

The data that support the findings of this study are openly available in Zendo at [52].

ACKNOWLEDGMENTS

The authors thank SNSF for financial support via Grant No. 177550. We acknowledge discussions with A. Mucchietto, M. Mruczkiewicz, S. Nikitov, and A. Sadovnikov. The different pieces of the hematite crystal were provided by J.-P. Ansermet and M. Bialek. We thank them for the support and discussions. The scientific color maps developed by Crameri *et al.* [53] is used in this study to prevent visual distortion of the data and exclusion of readers with color-vision deficiencies [54].

[1] V. V. Kruglyak, S. O. Demokritov, and D. Grundler, J. Phys. D: Appl. Phys. **43**, 264001 (2010).
[2] A. Barman, G. Gubbiotti, S. Ladak, A. O. Adeyeye, M. Krawczyk, J. Grafe, C. Adelmann, S. Cotofana, A. Naeemi, V. I. Vasyuchka, B. Hillebrands, S. A. Nikitov, H. Yu, D. Grundler, A. V. Sadovnikov, A. A. Grachev, S. E. Sheshukova, J. Y. Duquesne, M. Marangolo, G. Csaba, W. Porod, V. E. Demidov, S. Urazhdin, S. O. Demokritov, E. Albisetti, D. Petti, R. Bertacco, H. Schultheiss, V. V. Kruglyak, V. D. Poimanov, S. Sahoo, J. Sinha, H. Yang, M. Münzenberg, T. Moriyama, S. Mizukami, P. Landeros, R. A. Gallardo, G. Carlotti, J. V. Kim, R. L. Stamps, R. E. Camley, B. Rana, Y. Otani, W. Yu, T. Yu, G. E. Bauer, C. Back, G. S. Uhrig, O. V. Dobrovolskiy, B. Budinska, H. Qin, S. Van Dijken, A. V. Chumak, A. Khitun, D. E. Nikonov, I. A. Young, B. W. Zingsem, and M. Winklhofer, J. Phys.: Condens. Matter **33**, 413001 (2021).
[3] K. Baumgaertl and D. Grundler, Nat. Commun. **14**, 1490 (2023).
[4] V. S. Tkachenko, A. N. Kuchko, M. Dvornik, and V. V. Kruglyak, Appl. Phys. Lett. **101**, 152402 (2012).
[5] K. Vogt, H. Schultheiss, S. Jain, J. E. Pearson, A. Hoffmann, S. D. Bader, and B. Hillebrands, Appl. Phys. Lett. **101**, 042410 (2012).
[6] S. Mieszczak, O. Busel, P. Gruszecki, A. N. Kuchko, J. W. Kłos, and M. Krawczyk, Phys. Rev. Appl. **13**, 054038 (2020).
[7] D. C. Doughty and E. A. D. White, Acta Cryst. **13**, 761 (1960).
[8] A. A. Serga, A. V. Chumak, and B. Hillebrands, J. Phys. D: Appl. Phys. **43**, 264002 (2010).
[9] M. Sparks, R. Loudon, and C. Kittel, Phys. Rev. **122**, 791 (1961).
[10] S. Maendl, I. Stasinopoulos, and D. Grundler, Appl. Phys. Lett. **111**, 012403 (2017).
[11] H. Yu, O. D'Allivy Kelly, V. Cros, R. Bernard, P. Bortolotti, A. Anane, F. Brandl, F. Heimbach, and D. Grundler, Nat. Commun. **7**, 11255 (2016).
[12] K. Baumgaertl, J. Gräfe, P. Che, A. Mucchietto, J. Förster, N. Träger, M. Bechtel, M. Weigand, G. Schütz, and D. Grundler, Nano Lett. **20**, 7281 (2020).
[13] P. Che, K. Baumgaertl, A. Kúkol'ová, C. Dubs, and D. Grundler, Nat. Commun. **11**, 1445 (2020).
[14] A. V. Chumak, A. A. Serga, and B. Hillebrands, J. Phys. D: Appl. Phys. **50**, 244001 (2017).
[15] E. Turov, J. Exp. Theor. Phys. **9**, 890 (1959).
[16] F. Keffer, *Spin Waves*, edited by H. P. J. Wijn (Springer, Berlin, 1966), pp. 1–273.
[17] E. J. Samuelsen and G. Shirane, Phys. status solidi **42**, 241 (1970).
[18] J. R. Hortensius, D. Afanasiev, M. Matthiesen, R. Leenders, R. Citro, A. V. Kimel, R. V. Mikhaylovskiy, B. A. Ivanov, and A. D. Caviglia, Nat. Phys. **17**, 1001 (2021).
[19] C. Sirtori, Nature (London) **417**, 132 (2002).
[20] I. S. Osborne, Science **320**, 1262b (2008).
[21] A. H. Morrish, *Canted Antiferromagnetism: Hematite* (World Scientific, Singapore, 1995).
[22] M. Hamdi, F. Posva, and D. Grundler, *67th Annu. Conf. Magn.* (2022), pp. 229, GOE–12.
[23] H. Wang, R. Yuan, Y. Zhou, Y. Zhang, J. Chen, S. Liu, H. Jia, D. Yu, J.-P. Ansermet, C. Song, and H. Yu, Phys. Rev. Lett. **130**, 096701 (2023).
[24] R. Lebrun, A. Ross, S. A. Bender, A. Qaiumzadeh, L. Baldrati, J. Cramer, A. Brataas, R. A. Duine, and M. Kläui, Nature (London) **561**, 222 (2018).
[25] R. Lebrun, A. Ross, O. Gomonay, V. Baltz, U. Ebels, A. L. Barra, A. Qaiumzadeh, A. Brataas, J. Sinova, and M. Kläui, Nat. Commun. **11**, 6332 (2020).
[26] H. Wang, Y. Xiao, M. Guo, E. Lee-Wong, G. Q. Yan, R. Cheng, and C. R. Du, Phys. Rev. Lett. **127**, 117202 (2021).
[27] P. Pincus, Phys. Rev. Lett. **5**, 13 (1960).
[28] J. O. Artman, J. C. Murphy, and S. Foner, Phys. Rev. **138**, A912 (1965).

[29] C. W. Searle and S. T. Wang, J. Appl. Phys. **39**, 1025 (1968).
[30] M. Shone, Circuits Syst. Signal Process. **4**, 89 (1985).
[31] S. Watanabe, V. S. Bhat, K. Baumgaertl, M. Hamdi, and D. Grundler, Sci. Adv. **7**, eabg3771 (2021).
[32] B. M. Moskowitz, M. Jackson, and V. Chandler, in *Geophysical Properties of the Near-Surface Earth: Magnetic Properties: Treatise on Geophysics*, 2nd ed., edited by G. Schubert (Elsevier, Amsterdam, 2015), Vol. 11, Chap. 11.05, pp. 139–174.
[33] B. Iandolo, B. Wickman, I. Zorić, and A. Hellman, J. Mater. Chem. A **3**, 16896 (2015).
[34] A. H. Hill, F. Jiao, P. G. Bruce, A. Harrison, W. Kockelmann, and C. Ritter, Chem. Mater. **20**, 4891 (2008).
[35] J. Eaton, A. Morrish, and C. Searle, Phys. Lett. A **26**, 520 (1968).
[36] J. A. Eaton and A. H. Morrish, J. Appl. Phys. **40**, 3180 (1969).
[37] J. A. Eaton and A. H. Morrish, Can. J. Phys. **49**, 2768 (1971).
[38] Ö. Özdemir and D. J. Dunlop, J. Geophys. Res. Solid Earth **111**, B12S03 (2006).
[39] Ö. Özdemir and D. J. Dunlop, J. Geophys. Res. Solid Earth **119**, 2582 (2014).
[40] SurfaceNet GmbH, https://surfacenet.de/files/start.php
[41] M. Bialek, J. Zhang, H. Yu, and J. P. Ansermet, Appl. Phys. Lett. **121**, 032401 (2022).
[42] H. J. Fink, Phys. Rev. **133**, A1322 (1964).
[43] M. R. Querry, *Optical Constants*, Tech. Rep., Missouri University, 1984.
[44] T. Sebastian, K. Schultheiss, B. Obry, B. Hillebrands, and H. Schultheiss, Front. Phys. **3**, 35 (2015).
[45] L. Novotny and B. Hecht, *Principles of Nano-Optics* (Cambridge University Press, Cambridge, 2012), p. 584.
[46] U. Levy, N. Davidson, and Y. Silberberg, Adv. Opt. Photon. **11**, 828 (2019).
[47] S. S. Kalarickal, P. Krivosik, M. Wu, C. E. Patton, M. L. Schneider, P. Kabos, T. J. Silva, and J. P. Nibarger, J. Appl. Phys. **99**, 093909 (2006).
[48] C. Bilzer, T. Devolder, P. Crozat, C. Chappert, S. Cardoso, and P. P. Freitas, J. Appl. Phys. **101**, 074505 (2007).
[49] H. Yu, O. d'Allivy Kelly, V. Cros, R. Bernard, P. Bortolotti, A. Anane, F. Brandl, R. Huber, I. Stasinopoulos, and D. Grundler, Sci. Rep. **4**, 6848 (2014).
[50] R. Z. Levitin, A. S. Pakhomov, and V. A. Shchurov, J. Exp. Theor. Phys. **29**, 669 (1969).
[51] P. P. Maksimenkov and V. I. Ozhogin, J. Exp. Theor. Phys. **38**, 324 (1974).
[52] M. Hamdi, F. Posva, and D. Grundler, "Spin wave dispersion of ultra-low damping hematite (α-Fe_2O_3) at GHz frequencies", https://doi.org/10.5281/zenodo.7966466 (2023).
[53] F. Crameri, https://zenodo.org/record/5501399
[54] F. Crameri, G. E. Shephard, and P. J. Heron, Nat. Commun. **11**, 5444 (2020).